Flexural performance of reinforced concrete beams damaged by Alkali-Silica Reaction

Pierre Morenon, Stéphane Multon, Alain Sellier, Etienne Grimal, Francois Hamon, Philippe Kolmayer

Flexural performance of reinforced concrete beams damaged by Alkali-Silica Reaction

Pierre Morenon[1*], Stéphane Multon[1], Alain Sellier[1], Etienne Grimal[2], François Hamon[3], Philippe Kolmayer[2]

[1]LMDC, Université de Toulouse, INSA/UPS Génie Civil, 135 Avenue de Rangueil, 31077 Toulouse cedex 04, France

[2]Electricité de France, Centre d'Ingénierie Hydraulique, EDF-CIH Technolac, 73373 Le Bourget du Lac Cedex, France

[3]EDF Lab Paris – Saclay, 7 boulevard Gaspard Monge, 91120 Palaiseau, France

Abstract

Alkali-Silica Reaction (ASR) affects concrete and decreases its mechanical characteristics. However, for some reinforced concrete structures, the global mechanical behaviour can appear to be improved by ASR: for similar reinforcement, the first flexural cracking of reactive beams usually occurs for higher loading than in non-reactive beams. The flexural failures of two reinforced beams, one reactive and one non-reactive, are numerically simulated here in order to discuss the origins of the delay in cracking observed for the reactive beam. The poromechanical model used considers the swelling anisotropy, and is able to differentiate ASR diffuse cracking from structural macrocracks and the coupling of both crack

[*] Corresponding author. E-mail address: morenon@insa-toulouse.fr (P. Morenon). LMDC, Université de Toulouse, INSA/UPS Génie Civil, 135 Avenue de Rangueil, 31077 Toulouse cedex 04 France

Tel.: +33 5 61 55 99 16 - Fax. : +33 5 61 55 99 49.

types with creep. According to the model results, the cracking delay is due to the chemical prestress in the concrete induced by the ASR swelling being restrained in the direction of the reinforcements; the concrete has to be decompressed before cracking. The mechanical modelling presented in the paper is able to reproduce the differences between the reactive beam and the reference one. The cracking delay obtained for the ASR beam in the flexural test seems interesting from the mechanical point of view. However, this performance could be counterbalanced by durability problems due to ASR diffuse cracking that is induced parallel to the reinforcements. In fact, these cracks, also evaluated by the present modelling, are privileged paths for the ingress of deleterious agents such as carbonates or chlorides.

Keywords: Alkali-Silica Reaction (ASR), flexural mechanical behaviour, reinforced concrete, modelling, diffuse cracking, localized macrocracks.

1. Introduction

Alkali-Silica Reaction (ASR) affects the concrete of structures such as dams, bridges or basements [1–3]. This internal swelling reaction generates damage in the material, which can lead to a degradation of the concrete characteristics and the structure stability. However, the behaviour of some reinforced structures seems to be improved by ASR [4–7]. In flexion, the first cracking occurs for higher loading if the beam has undergone AAR. To consider this phenomenon in structural analysis, a numerical approach is proposed and confronted with the behaviour of real beams.

In this context, a faithful cracking model is essential. Usually, two kinds of tensile cracking are observed in concrete structures affected by ASR. The first is ASR diffuse cracking, which leads to decreases in the material characteristics (tensile and compressive strengths, elastic modulus) [8–10]. The second kind of cracking is localized structural cracks. This can come from external loads as in all structures. It is also encountered in ASR-affected

structures because of swelling gradients [11]. The hydric state and the alkali release rate influence the swelling kinetics and amplitude through the structure. This can induce significant swelling gradients and thus tensile stresses and localized cracks. According to their opening, such cracks can lead to stress concentrations in steel bars (reinforcement), and to water leaks or durability problems. Cracks are an open door to aggressive agents such as CO_2 or chlorides.

To obtain accurate assessments of damaged structures and, in particular, to determine the failure mode of a structure and its durability, mechanical modelling should be able to differentiate between diffuse cracking and localized cracks. Therefore, two distinct criteria need to be defined: one for diffuse cracking of the material and one for structural localized cracking. Moreover, as the calculations have to be performed over a long time scale, all the delayed deformations should be evaluated. In particular, concrete creep has to be taken into account to obtain reliable stress evaluation for structures damaged by ASR over several decades.

The first part of this paper presents the main features of the model. This type of modelling, clarified and implemented in several finite element software products since 1997 [12], has been continuously improved and is now able to clearly differentiate diffuse and localized damage and to combine these two kinds of damage with creep. The second part of the paper is the application of the model to a flexural test to failure on laboratory reinforced beams (with and without ASR) in two phases: the service life (ageing, also modelled by [13–15]) and the residual strength (failure test, never modelled). The comparison of force-deflection curves leads to a discussion on the impact of ASR, on the flexural performance of these structures and on their durability.

2. Modelling

2.1. Rheological model

The concrete behaviour law is established in the poromechanical framework. The rheological model is built to accept the two kinds of cracking (Figure 1) that are encountered in structures affected by ASR. The first one is ASR diffuse cracking, which is a direct consequence of the ASR gel pressure inside the material (Figure 1) at the microscopic scale. The structural localized cracks are evaluated separately (Figure 1). The creep is also taken into account by Sellier's model, which contains a Kelvin-Voigt (visco-elastic) and an anisotropic non-linear Maxwell level in order to reproduce multi-axial delayed strains due to loading [16]. The model takes into account creep reversibility and irreversibility, nonlinearity with stress, anisotropy, dependence to moisture and temperature to be as realistic as possible and usable in structural calculations [16]. The rheological model uses a poromechanical scheme to take ASR gel pressure, water pressure (shrinkage), and external stress into account in the creep calculation. This global scheme directly couples the concrete swelling and the tensile creep produced around the reactive sites [17].

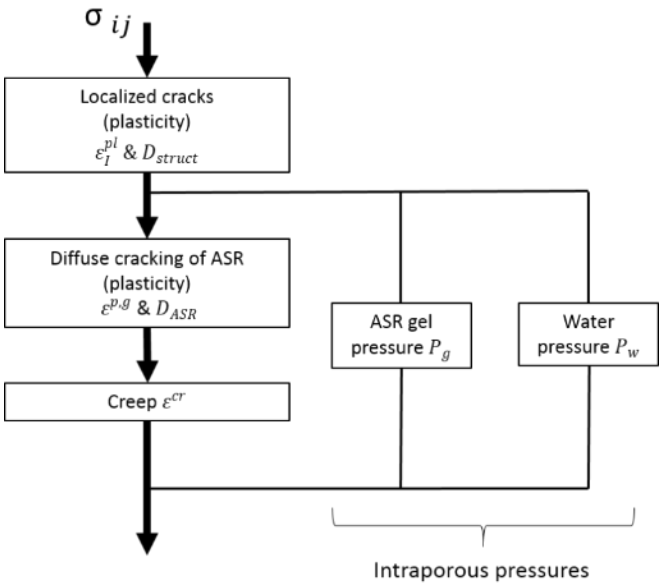

Figure 1: Rheological model

In Figure 1, the total stress σ_{ij} is calculated from the damage D_{ASR} (due to ASR) and D_{struct} (due to structural cracks), and from the effective stress $\tilde{\sigma}_{ij}$ (Equation (1)). In the context of damage theory, the effective stress $\tilde{\sigma}_{ij}$ corresponds to the stress in the undamaged zone of the material, which itself can be defined in the framework of poromechanics theory [18] by Equation (2) [16], with $\tilde{\sigma}_{ij}{}'$ the stress part in the solid and $(-b_g\ P_g - b_w\ P_w)$ the contribution of the interstitial phase pressures (P_g for the pressure due to ASR and P_w for the pressure due to shrinkage induced by water). Each interstitial pressure is affected by the corresponding Biot coefficient (respectively b_g and b_w [19]). δ_{ij} is the Kronecker symbol, equal to 1 only if $i = j$. The effective poromechanical stress increment $\dot{\tilde{\sigma}}_{ij}{}'$ is calculated from the stiffness matrix S_0 and the elastic strain. The elastic strains can be obtained by subtracting the non-elastic strain increments ($\dot{\varepsilon}_{pl\,kl}$ for the plastic strain, $\dot{\varepsilon}_{cr\,kl}$ for the creep strain and $\dot{\varepsilon}_{th\,kl}$ for the thermal strain) from the total strain increment $\dot{\varepsilon}_{kl}$ according to Equation (3).

$$\sigma_{ij} = (1 - D_{ASR})\ (1 - D_{struct})\ \tilde{\sigma}_{ij} \qquad (1)$$

$$\tilde{\sigma}_{ij} = \tilde{\sigma}_{ij}' - \delta_{ij}\, b_g\, P_g - \delta_{ij}\, b_w\, P_w \quad (2)$$

$$\dot{\tilde{\sigma}}_{ij}' = S_0\, (\, \dot{\varepsilon}_{kl} - \dot{\varepsilon}_{pl\,kl} - \dot{\varepsilon}_{cr\,kl} - \dot{\varepsilon}_{th\,kl}\,) \quad (3)$$

95

96 *2.2. ASR diffuse cracking*

97 ASR-gel pressure P_g creates an orthoradial tensile stress around each reaction site (Figure 2)
98 When the tensile strength, $R_{t\,micro}$, is reached at this microscale, diffuse cracking begins and
99 leads to the decrease of macro material characteristics such as the elastic modulus [20,21].
100 This cracking (ASR cracking) is diffuse because it can develop at the level of each reactive
101 swelling site [22]. It can be oriented according to the multi-axial stress state [17], which
102 depends on the external stress applied, $\tilde{\sigma}_I$. The ASR plastic criteria are described below.

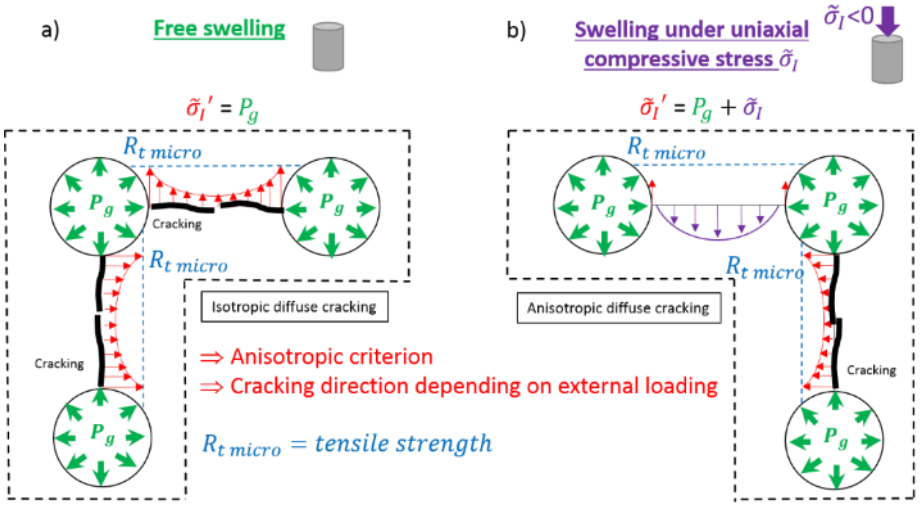

103

104 **Figure 2: Scheme of the ASR plastic criterion for free swelling (a) and swelling under**
105 **uniaxial compressive stress (b)**

106 Details of the numerical implementation algorithm used to combine the poromechanics, the
107 creep, the plastic flow and the orthotropic damage occurrences are available in [23]. Only the
108 main features of this implementation are presented here.

2.2.1. Chemical advancement

The evolution of the gel pressure depends on the ASR chemical advancement, A^{asr}. In this work, the advancement is evaluated from an empirical equation (4) already used by [24]. It depends on:

- a characteristic time τ_{ref}^{asr} , calibrated using a free swelling test,
- two coefficients to take account of environmental impacts:
  - one for the temperature effect, $C^{T,asr}$, managed by an Arrhenius law (5) (E^{asr} is the thermal activation energy (≈ 40,000 J.Mol^{-1} [25]), R is the perfect gas constant (8.3145 J.mol^{-1} K^{-1}), and T_{ref} is the temperature corresponding to the τ_{ref}^{asr} calibration),
  - one for the humidity effect, $C^{W,asr}$(6), proposed in [17] based on Poyet's law [26]. It uses a minimum threshold to initiate the reaction $S_r^{th,asr}$ (here 0.1) and evolves non-linearly in order to strongly accelerate the reaction kinetics with the water saturation of the material.
- a kinetics and amplitude term $< Sr - A^{asr} >^{+}$, which limits the advancement at the saturation degree Sr, following the conclusion of [26].

Water has two main roles in ASR gel formation: it can be absorbed by ASR products and it allows the diffusion of ionic species necessary for aggregate attack and products precipitation. That is the reason why the lack of water in the porosity stops the chemical reactions; hydroxyl ions do not come into contact with the silica in the aggregates. The effect of water on the chemical reaction is taken into account in equation (4) by means of the porosity saturation ratio (Sr). For low saturation degrees, aggregate attack cannot occur and the chemical advancement is stopped. Therefore, the gel volume does not reach its total amplitude.

$$\frac{\delta A^{asr}}{\delta t} = \frac{1}{\tau_{ref}^{asr}} C^{T,asr} C^{W,asr} < Sr - A^{asr} >^{+} \quad (4)$$

$$C^{T,asr} = \exp\left(-\frac{E^{asr}}{R}\left(\frac{1}{T} - \frac{1}{T_{ref}}\right)\right) \quad (5)$$

$$C^{W,asr} = \begin{cases} \left(\frac{S_r - S_r^{th,asr}}{1 - S_r^{th,asr}}\right)^2 & if \quad S_r > S_r^{th,asr} \\ 0 & if \quad S_r \leq S_r^{th,asr} \end{cases} \quad (6)$$

2.2.2. Gel pressure

Then, the balance of solid and liquid volumes changes due to ASR is noted ϕ_g (7). It is obtained from the ASR advancement, A^{asr}, and from the balance of volume change ϕ_g^{∞} corresponding to the total reaction. The relatively simple equations set (4-8) are usually sufficient to obtain relevant representation of water effects on samples and for structural modelling [13,26].

$$\phi_g = \phi_g^{\infty} . A^{asr} \quad (7)$$

The production of gels by ASR leads to increasing the pressure around the reaction site. It can induce cracking in the aggregate and / or in the cement paste depending on aggregate nature [29]. The intra-porous pressure induced by the ASR gel, P_g , (Figure 2) is calculated with a matrix-gel interaction modulus M_g (taken equal to 27 700 MPa according to [17]) and from the volume of ASR gel, ϕ_g:

$$P_g = M_g < \phi_g - \left(\underbrace{\phi_g^v \left(\frac{P_g}{\tilde{R}_I^t}\right)}_{\phi 1} + \underbrace{b_g tr(\varepsilon^e + \varepsilon^{cr})}_{\phi 2} + \underbrace{tr(\varepsilon^{p,g})}_{\phi 3} \right) >^{+} \quad (8)$$

In this equation, the volumes $\phi 1$, $\phi 2$ and $\phi 3$ can impact the evolution of the pressure for mechanical and / or chemical reasons:

1) A part of the gel produced by ASR, $\phi 1$, migrates into the porosity inside the aggregate and/or the concrete (according to the aggregate nature) [30–32]. In this work, it is taken to depend on a characteristic void volume, ϕ_g^v (calibrated in a free swelling test), on the gel pressure applied, P_g, (the higher the pressure is, the greater is the reachable volume of connected porosity, as in a Hg intrusion test [33]), and on the effective tensile strength, $\tilde{R}_I^t$. The increase of the proportion of gel that permeates into the porosity connected to the reaction site with increasing pressure can thus be evaluated without supplementary equations. It is especially necessary to model the expansion under multi-axial compression due to external loadings [34].
2) The volume of porosity is modified by the strains induced by external loading. Positive strains lead to a decrease of the pressure while negative strains lead to a pressure increase. It is evaluated from $\phi 2$. b_g is the Biot coefficient, which comes from the poromechanics, and $tr(\varepsilon^e + \varepsilon^{cr})$ is the volume induced by the elastic and the creep strains ("$tr(\,)$" represents the matrix trace). Creep and swelling are thus strongly coupled.
3) In this work, the volume of diffuse cracking is evaluated from the plastic strains $tr(\varepsilon^{p,g})$. The behaviour law of ASR products (8), considers the effects of these microcracking as permanent strains of the matrix. Even if the term $\phi 3$ in equation (8) assumes that the microcracks are completely filled by the ASR products, microscopic observations show that in reality they are only partially filled [35]; this simplification assumption is balanced by the fitting of ϕ_g^∞ which is chosen to minimize model deviation toward real swelling, the consequence is that ϕ_g^∞ certainly includes also a volume fraction of empty micro-cracks induced by ASR. This pressure model configuration seems sufficient to model mechanical behaviour of ASR samples and beams without resorting to more complex models of ASR diffusion or aging, what limits the parameters number.

2.2.3. ASR plastic criteria

For a free swelling concrete, when the gel pressure P_g causes an orthoradial tensile stress equal to the strength $R_{t\,micro}$ in the vicinity of the reactive spots, the diffuse cracking due to ASR begins. The criterion (9) written for each main tensile stress direction, depends on the external loading, $\tilde{\sigma}_I$, through the effective stress, $\tilde{\sigma}_I{}'$ (10). If the concrete is free to swell, the criterion is activated when P_g reaches $R_{t\,micro}$. If the concrete is under an external compressive stress, in direction I for instance, the criterion will be reached first for a pressure equal to $R_{t\,micro}$ in directions II and III. This implies that diffuse cracking propagates in the planes perpendicular to these two directions while cracking in the plane perpendicular to the direction I (Figure 2) is delayed or impeded. In direction I, the pressure has to rise to $R_{t\,micro}$ plus the intensity of the compressive stress $\tilde{\sigma}_I$ to cause diffuse cracking (Equation (10) in (9)).

$$f_I^{t\,ASR} = \tilde{\sigma}_I{}' - R_{t\,micro} \quad I \in [I, II, III] \tag{9}$$

$$\tilde{\sigma}_I{}' = P_g + \min(\tilde{\sigma}_I\,; 0\,) \quad I \in [I, II, III] \tag{10}$$

Once the criterion is reached in one direction, a plastic strain $\varepsilon_I^{p,g}$ is induced. This plastic strain represents the diffuse cracking due to ASR.

2.2.4. ASR damage

Anisotropic tensile damage, $D_I^{t,g}$, due to gel pressure in the three principal directions, is deduced from the corresponding ASR plastic strains $\varepsilon_I^{p,g}$ in each main cracking direction ((11) from [36]) and from a characteristic strain $\varepsilon^{k,g}$. The characteristic strain is taken as constant and equal to 0.3 % [37].

$$D_I^{t,g} = \frac{\varepsilon_I^{p,g}}{\varepsilon_I^{p,g} + \varepsilon^{k,g}} \tag{11}$$

2.3. Localized cracks

188 Localized cracks can be caused by external loads or ASR swelling gradients, due to
189 humidity or alkali transfers for instance. They can lead to leakage, reinforcement stress
190 concentration and decreased durability. This part describes the model used to reproduce the
191 concrete behaviour in tension and particularly for the determination of the localized cracks
192 induced by the structural effects. This cracking is always oriented perpendicular to the
193 principal tensile directions.

194 *2.3.1. Rankine plastic criterion*

195 To consider the behaviour of concrete in tension, the model [23] associates plasticity
196 and damage theory [38,39]. The initialization of localized cracks is managed by an anisotropic
197 Rankine plastic criterion (Equation (12) from [40]). Numerically, the hypothesis is that up to
198 three orthogonal localized cracks can exist for each finite element. During a test in direct
199 tension, the apparent stress $\tilde{\sigma}_I$ increases until the tensile strength R_I^t is reached (Figure 3, point
200 ①) for the peak strain ε_{peak}^t. This path could be linear (perfect elasticity with E the elasticity
201 modulus) or nonlinear (diffuse damage $D_{priorpeak}$ before the peak). In the latter case, the
202 effective stress at the peak, $\tilde{R}_I^t$, as defined in damage theory, is greater than the tensile
203 strength R_I^t that can be measured on the concrete (13). The difference between the effective
204 stress at the peak, $\tilde{R}_I^t$, and the measured tensile strength, R_I^t, is due to the damage occurring
205 before the peak, which characterizes the nonlinearity of the tensile behaviour of concrete
206 before the peak. Details about this part of the model are available in [41]. The prior peak
207 damage $D_{priorpeak}$ is maximum at that point and is equal to D_{peak} (14).

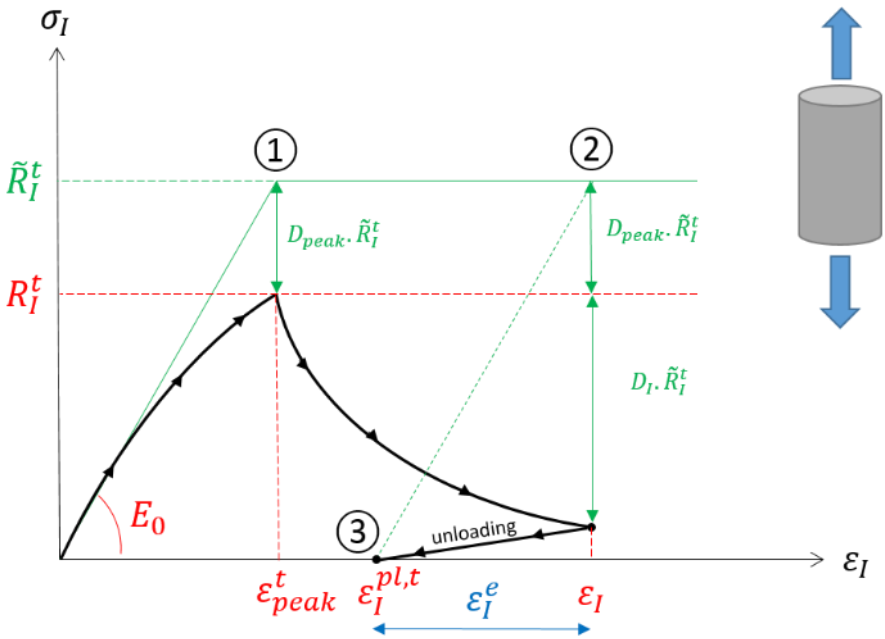

208

209 **Figure 3: Model of concrete tensile behaviour under external loading or displacement**
210 **gradients**

$$f_I^{t\,struct} = \tilde{\sigma}_I - \tilde{R}_I^t \tag{12}$$

$$\tilde{R}_I^t = \frac{R_I^t}{(1 - D_{priorpeak})} \tag{13}$$

$$D_{peak} = \frac{R_t}{E.\varepsilon_{peak}^t} \tag{14}$$

211 *2.3.2. Plastic strain and damage*

212 After the peak (Figure 3), the concrete behaviour is managed by a theory of plastic
213 flow coupled with anisotropic damage. When the strain is higher than the peak tensile strain,
214 ε_{peak}^t, a localized crack is assumed to be initiated in the finite element. For any strain (Figure
215 3, point ②), the total stress is calculated from the peak damage D_{peak} and the localized
216 damage in the corresponding main direction D_I^{struct} ((15) and (16)). w_I^k is a characteristic
217 crack opening (calculated to dissipate the fracture energy Gft). $w_I^{pl,max}$ is the maximal value
218 of the crack opening in the principal direction I, obtained from the maximal plastic strain
219 $\varepsilon_I^{pl,max}$ multiplied by the finite element size in this direction.

$$\sigma_I = \left(1 - D_{peak}\right)\left(1 - D_I^{struct}\right)\tilde{\sigma}_I \quad (15)$$

$$D_I^{struct} = 1 - \left(\frac{w_I^k}{w_I^k + w_I^{pl,max}}\right)^2 \quad (16)$$

An energy regularization is necessary for the post-peak behaviour law where the localized crack occurs. Here, the continuous Hillerborg method [42] is used to adapt the volumetric dissipated energy and obtain a constant surface energy.

2.4. Combining diffuse cracking and localized cracks

Diffuse cracking and localized cracks are combined through the weakest link method. The effective stress $\tilde{\sigma}_I$ (12) is affected by the ASR diffuse cracking $D_I^{t,g}$ in this direction (17) (for the sake of simplicity no prior peak damage is considered here).

$$\tilde{\sigma}_I = \left(1 - D_I^{t,g}\right)\left(1 - D_I^{struct}\right)\sigma_I \quad (17)$$

For a direct tensile test, the tensile stress is lower on a sample affected by ASR than on a sound one (Figure 4). In this model, the ASR damage has the same impact on the effective stress and on the effective modulus.

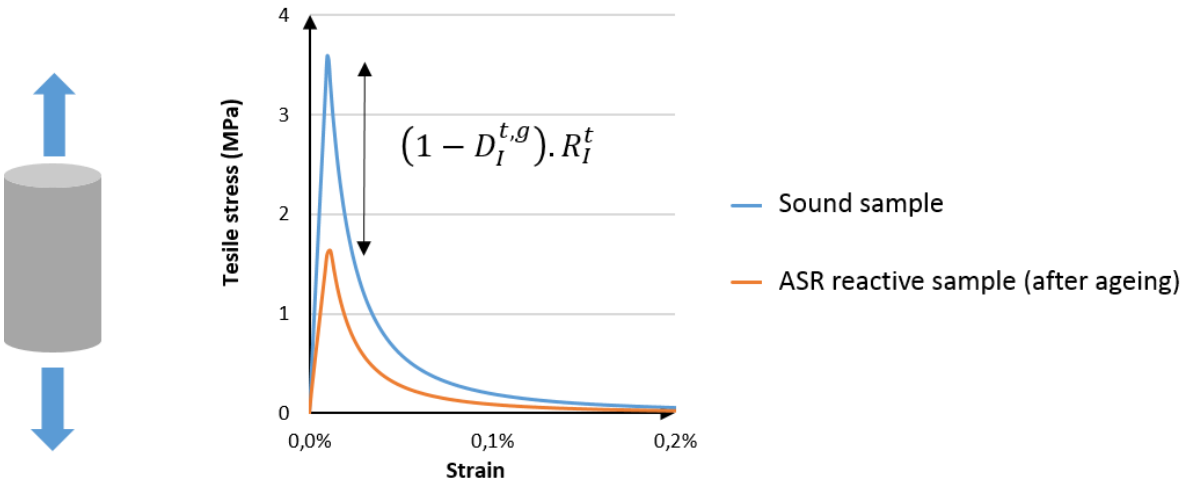

Figure 4: ASR cracking and localized crack combinations

3. Ageing simulation of laboratory structures

Based on the validation of the coupling between diffuse cracking and creep presented in [17], the model is applied to a flexural failure test carried out on reinforced concrete beams (with and without ASR) in two phases: the service life (ageing) and the residual strength (failure test) [6,7,43,44]. The model responses and the experimental results are compared for the displacements and the cracking patterns of the beams. The effects of reinforcement on swelling and on stress induced in the reinforced beams are analysed in comparison with a beam without reinforcement that is also damaged by ASR in the same conditions.

3.1. Methodology and test conditions

All the experimental results analysed in this section are taken from Multon's work [6,44,7,43]. The concrete is the same as the one used for the multi-axial confinement samples that were studied with this model in [17]. Thus, the material parameters are the ones obtained in [17]. They are given in Table 1 and enable the deformations of the cylindrical specimens studied by Multon to be retrieved: shrinkage in non-saturated conditions, free swelling, and creep of sound and reactive specimens in both uniaxial and triaxial tests. The volumetric ASR gel potential ϕ_g^∞ (calibrated on a free swelling test) is about 0.54%. A part of this potential is supposed ineffective in Equation (8) (volume ϕ_g^v=0.13% in Table 1). Elastic, creep and ASR plastic strains used to obtain a relevant representation of ASR action on concrete in Equation (8) lead to the differences between the imposed volumetric ASR gel potential ϕ_g^∞ minus ϕ_g^v and the strains measured on concrete samples.

Table 1 : Material parameters calibrated on specimens in [17]

Parameter	Symbol	Value
General parameters		
Elastic modulus	E	37.2 MPa
Tensile strength	R^t	3.7 MPa
Fracture energy in tension	G_{ft}^t	1.0 10^{-4} MJ/m²

Compressive strength	R^c	38.3 MPa
ASR advancement		
ASR characteristic time	τ_{ref}^{asr}	105 days
Thermal activation energy	E^{asr}	40 000 J.Mol^{-1}
Saturation degree threshold	$S_r^{th,asr}$	0.1
Poromechanics		
Final volumetric gel potential	ϕ_g^{∞}	0.54%
Fraction of gel ineffective in creating expansion	ϕ_g^{v}	0.13%
Gel Biot coefficient	b_g	0.25
Gel Biot modulus	M_g	27 700 MPa
ASR diffuse cracking		
Plastic hardening ratio	h_{asr}	0.03

Three reactive beams are modelled in this part: one without reinforcement, one normally reinforced and one strongly reinforced. Their dimensions are 3.0 x 0.5 x 0.25 metres for 2.8 metres between supports. The lower 70 mm of the beams was immersed in water while their upper face was subjected to air-drying at 30% relative humidity (RH) for 428 days. No moisture transfer could occur on the lateral faces as they were covered with watertight aluminium. The upper faces were re-saturated with liquid water after 428 days (Figure 5) and saturation conditions were maintained for up to 700 days, while the boundary conditions in the other parts were not modified. The temperature was kept at 38 °C during the entire test. These beams were simply supported on steel bars 0.1 metre from each end and halfway up (Figure 5). Because of the double symmetry, only a quarter of the beam is modelled, to reduce the calculation time (Figure 5).

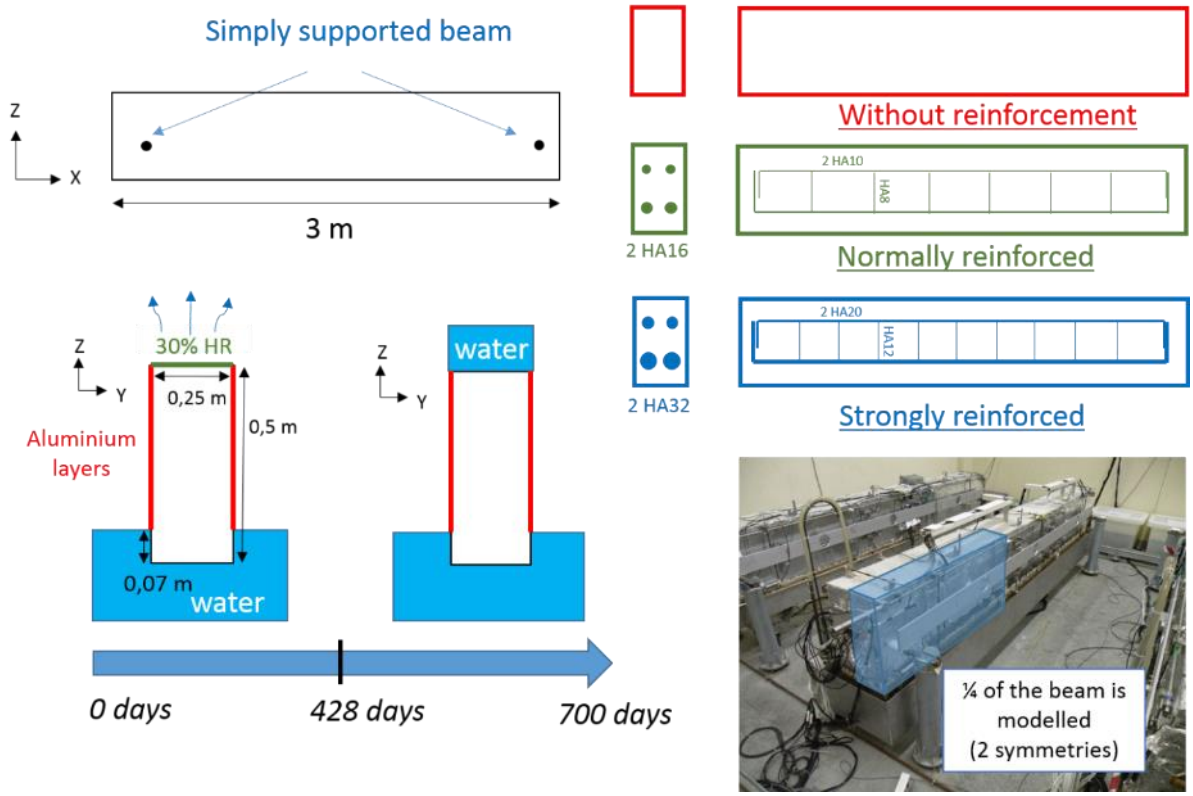

Figure 5: Geometry, limit conditions, environmental conditions and reinforcement of the beams [7,43]

The water saturation degree has a significant impact on the amplitude and the kinetics of ASR swelling. As the ASR-affected beams were subjected to hydric gradients here, a hydric calculation is necessary to reproduce the different swelling in the structures [45]. The calculations are chained: a hydric calculation is performed first and is followed by the poromechanics calculation. This chaining is possible because, on the one hand, the water pressure is mainly controlled by the desorption curve and not by liquid water compressibility and, on the other hand, the moisture transfer is driven by capillary forces in undamaged zones. The advantage of this chaining method is to separate the resolution of the different physical mechanisms (hydric and mechanical) and the drawback is that there is no feedback from the mechanical to the hydric state. In particular, the transfer is little modified by the cracking. A combination between mechanics and transfer based on Rahal's work [46,41] is a perspective of this work, which would improve the precision of the modelling response.

3.2. Beam meshes

The meshes used in the calculations are presented in Figure 6. The mesh of the non-reinforced beams is refined in the lower part to obtain accurate calculations in this area. For the reinforced beam, a finer mesh is used in the zones around the reinforcements to improve the modelling of the steel - concrete interface.

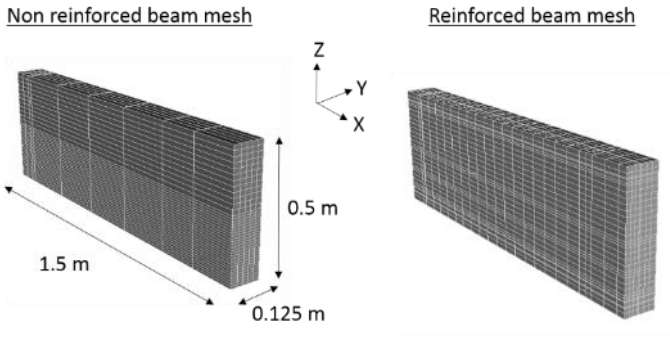

Figure 6: Meshes used

Elastic steels are used for the ageing calculation of the beams (Young's modulus of 200,000 MPa). In this modelling, induced swelling does not create plastic strains in steel bars. They are meshed as 1D bar elements (without thickness). For this validation step, no additional calibration is made. All the material parameters used are the parameters obtained on specimens cast with the same concrete and analysed in [17].

3.3. Determination of the water saturation degree in the structures

Alkali-silica reaction is very sensitive to the degree of saturation of the concrete [6,25,26,47]. The water facilitates the diffusion of the reactive species and contributes to the final volume of ASR-gels, which are hydrophilic. Accurate quantification is thus necessary to obtain relevant analysis.

To simulate drying (upper part) and capillary rise (lower part), a model of water diffusion is used (18). The water diffusion coefficient D (19) takes account of the permeation transfers

and the dependence of diffusion on the water saturation degree, W, according to Mensi's model [48]. This model is simple but it gives realistic representation of moisture gradients in the beams which is an important point for their structural analysis.

$$\frac{\delta W}{\delta t} - Div[D(W)\nabla W] = 0 \quad (18)$$

$$D(W) = a.e^{b.W} \quad (19)$$

The calibration is based on the data provided by the experimental programme [6,7]. For the coefficient a (equation (19)), the values vary between 1.2 10^{-13} $m^2.s^{-1}$ and 5.8 10^{-12} $m^2.s^{-1}$). The coefficient b is taken as 0.051 for the zone in imbibition and 0.06 for the zone under drying [13,49]. The profiles presented in Figure 7 for these two parameters have been evaluated to obtain a correct prediction of moisture transfers in the beams (Figure 8 and Figure 9). Variations between the top and the bottom of the beams can be due to differences in concrete porosity observed during the study [6]. Differences for parameter b between drying and rewetting are due to usual hysteresis behaviour between concrete sorption and desorption [50] and due to cracking appeared during the drying period. The initial saturation degree was determined on companion specimens made under the same conditions (degree of saturation 0.85 after 28 days of curing in endogenous conditions). The difficulty to use more precise modelling lies in the lack of experimental data, as sorption curves, to calibrate their parameters for the studied concrete. Thus, the total mass variation and water content profiles in the height of the structures are given in Figure 8 and in Figure 9. The evaluation of moisture in the depth of the beams is correct (Figure 9). This result gives confidence for the structural analysis.

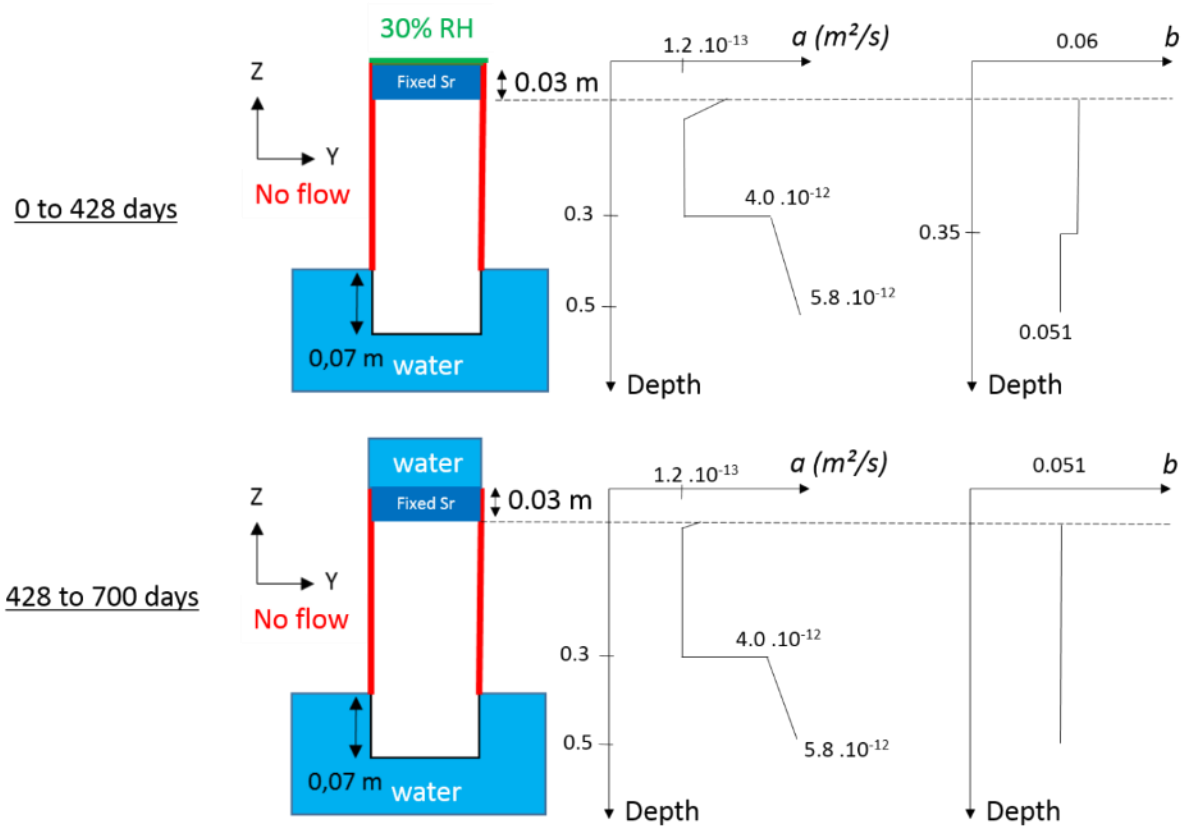

319

320 **Figure 7 : Boundary conditions for the hydric simulation and definitions of Mensi's law**
321 **coefficients *a* and *b***

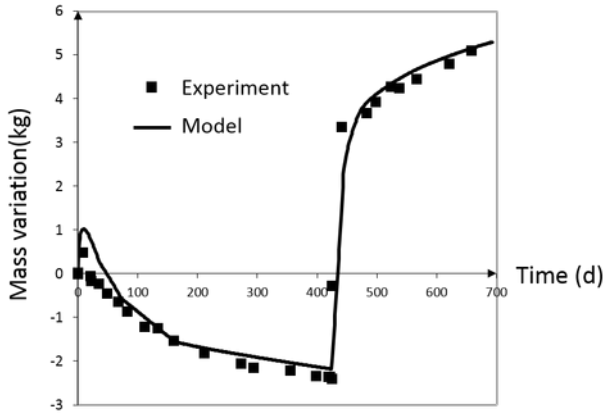

322

323 **Figure 8 : Experimental results of the mass variation of the non-reactive beam [43,44]**
324 **and modelling**

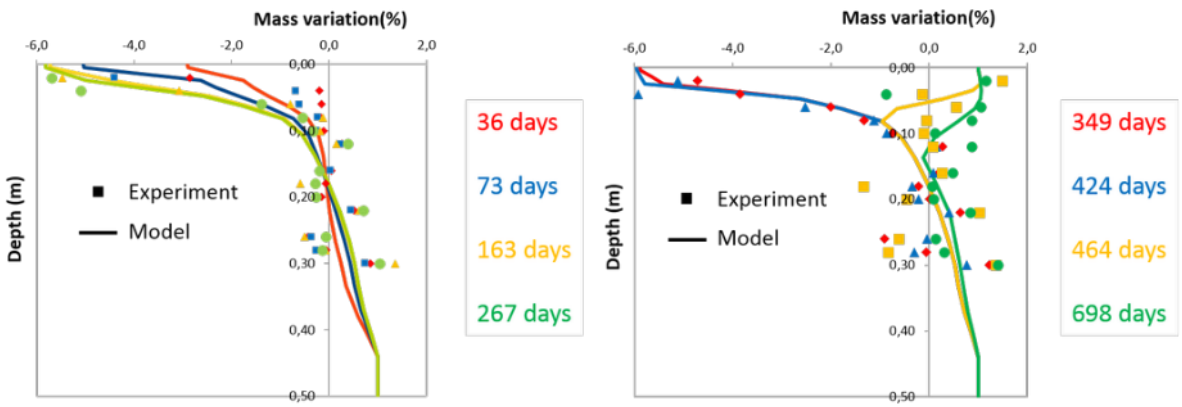

Figure 9 : Mass variation depending on the depth [43,44] and modelling

3.4. Structural behaviour modelling during ageing

3.4.1. Deflections

The results obtained by the modelling in terms of deflection at mid-span and mean longitudinal strain are compared to the experimental results for the three reactive beams in Figure 10. Deflection analysis is divided into two parts: before and after the wetting of the upper face (428 days) (Figure 10).

Imbibition-drying phase (before 428 days):

The deflections move towards negative values during the first 50 days because shrinkage in the upper part of the beams is the predominant phenomenon. Then, swelling is initiated in the lower part, which was immersed (Figure 10). In the reactive beam without reinforcement (WR red curve), the evolution of the deflection accelerates because the lower part of the beam is subjected to high positive strains while the upper part shortens slightly under the effect of shrinkage when drying. In the two reinforced beams, the longitudinal steel bars quickly restrain the ASR swelling in this direction. A compressive stress is then created in the concrete in the direction of the main reinforcements. The middle part (mid-height of the

beam) continues to swell with a delay due to the influence of the saturation degree on the ASR kinetics. It is the expansion in the middle part combined with the restraint of expansion by the steel bars that causes the inversion of the deflection evolution between 150 and 428 days.

For the amplitude, all the calculated deflections agree quite well with the experimental deflections obtained at the end of drying (428 days) as in [13–15].

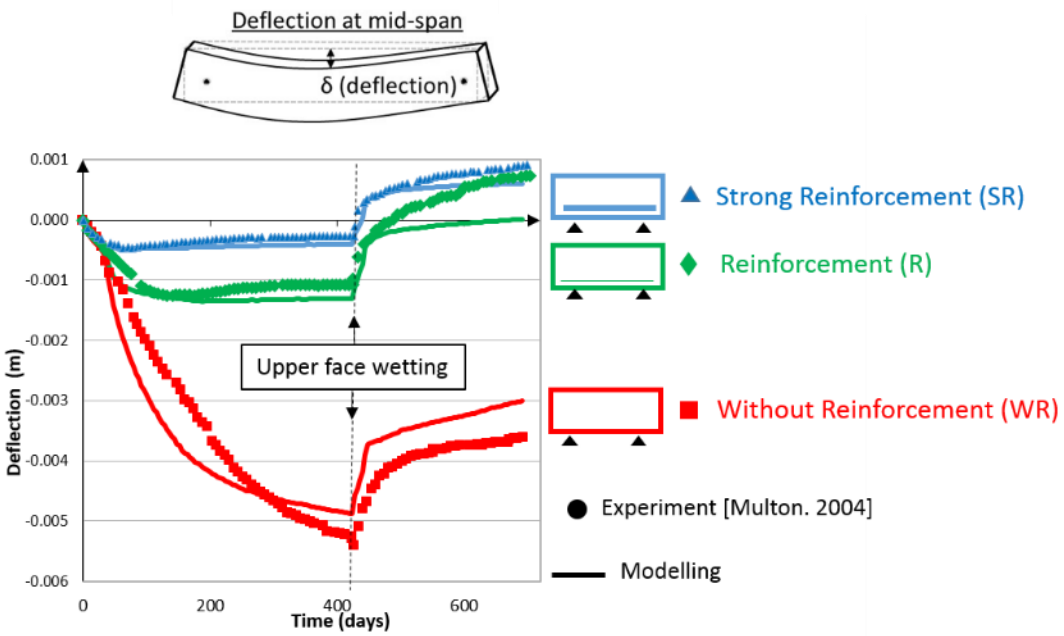

Figure 10: Comparison between deflections found in experimental data [43] and by modelling

Upper face wetting phase (after 428 days):

In this period, all beams moved upwards (positive deflection) as the upper face was then in contact with water. The upper part of the beams was saturated, implying a rapid positive deflection because the kinetics and the ASR swelling potential depend directly on the presence of water. In the case of late water supply, ASR can appear very quickly, as already discussed in [43]. The displacements are well reproduced by the model. The increase obtained during the upper face wetting seems to be managed in terms of amplitude. From 480 days, the deflections of the reinforced and strongly reinforced beams seem to evolve more slowly in the model than in reality. This can be due to the impact of transverse cracks caused by restrained

363 shrinkage obtained during the first 428 days in the upper part of the beam. The number of
364 these cracks is faithfully reproduced by the model for both beams but it is difficult to evaluate
365 the cracks depths and their impacts on hydric transfer during the rewetting. The differences
366 between calculation and experiment can be due to the absence of coupling between transfer
367 and mechanics. Indeed, the saturation degree modelling predict a fast and uniform rewetting
368 in the beams to fit the global mass balance while important rewetting could be localized
369 around cracks in the reality. It should not have the same structural consequences. The result is
370 a too fast stabilization of the deflection. This modelling could be improved in the future. All
371 these conclusions are confirmed by the comparison of longitudinal strains.
372 To prepare the failure bending tests on the normally reinforced beam, it is now interesting to
373 analyse its stress state at the end of the ageing phase.
374
375

376 *3.4.2. Stress state in the reinforced beam*

377 The influence of reinforcement on swelling and stress in concrete has a great impact on the
378 service and ultimate behaviours of damaged structures. This model faithfully reproduces the
379 impact of stresses and restraint on ASR expansions [17]. In the reinforced beams [6], the
380 swelling is restrained by the longitudinal steel bars. This causes tension in the steel bar and
381 compression in the concrete. The compressive stress obtained in concrete is comparable to a
382 chemical prestress [51,8,52]. With the isotropic gel pressure presented in the model, the
383 irreversible strain due to ASR in the unrestrained direction controls the gel pressure and, thus,
384 the prestress in the restrained direction.
385 Figure 11 represents a profile of the longitudinal stress in the height of the beam, obtained at
386 mid-span in the reinforced beam. Compressive stresses slightly higher than 2 MPa are
387 obtained by modelling. This is consistent with the results obtained in the first analysis

proposed by Multon et al. [53]. The main chemical prestresses are located in the areas close to the longitudinal reinforcement (the 200 mm closest to the lower face of the beam and within the 100 mm closest to the upper face). A maximum compressive stress of 2.2 MPa is obtained in the lower fibre.

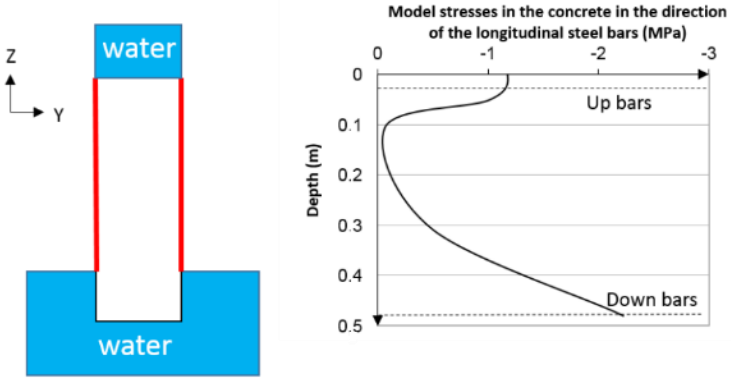

Figure 11: Computed stresses along elevation in the concrete in the longitudinal direction of the beam at mid span at 700 days

In the literature, this maximum chemical prestress obtained in contact with steels is estimated to be between 2 and 6 MPa [54–56,4]. The model presented here gives compression stresses between 0.7 and 3.3 MPa, depending on the reinforced directions (with or without stirrups) for a free ASR swelling of 0.3% [17]. Thus, flexural cracking can be delayed under applied loading due to the chemical prestress induced by ASR in reinforced structures. Experimentally, a reinforced wall subject to ASR can effectively crack later than a sound wall, thanks to this prestress [5].

In the reinforcement, the maximum stress (140 MPa) obtained by calculation is lower than the elastic limit of the steel (500 MPa). This is consistent with the structural analysis presented in [53]. The elastic behaviour of the steel bars during ageing is thus validated.

3.4.3. Effective mechanical characteristics of the normally reinforced beam

Figure 12 presents the damage due to ASR in the normally reinforced beam. The damage is variable in the beams and highly anisotropic due to the presence of the reinforcement. This is

due to the swelling anisotropy induced by the restraint of the steel bars [17]. The upper part of the beam is slightly affected by the ASR damage (<0.2) while the lower part is strongly affected in the directions parallel to the longitudinal steel bars (0.4 in the Y and Z directions). As a result, the concrete is little damaged perpendicular to the longitudinal direction. At the end of ageing, the elastic modulus and effective tensile strength are thus anisotropic and variable in the beam. This is the reason why the modulus measured on cores drilled from a structure may be not be representative of the mechanical behaviour of the structure as a whole. In the modelling, the mechanical properties are weighted by the ASR damage in each main direction in order to obtain realistic anisotropic values.

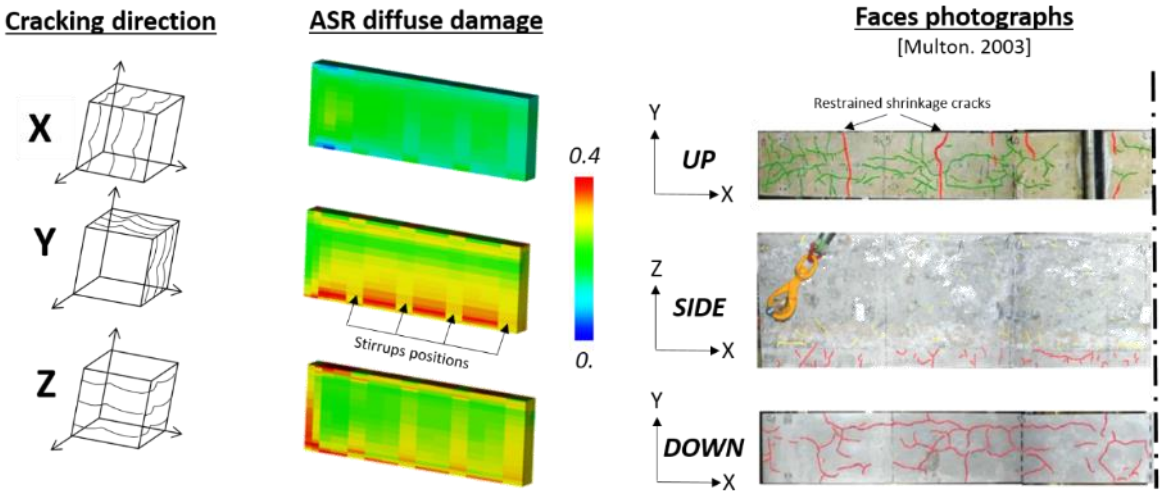

Figure 12: Comparison of cracking patterns obtained with the model and by experiment for the reinforced beam [6]

4. Simulation of behaviour up to failure of aged structures

4.1. Failure test set up

The failure test of the reinforced beams (one reactive and one non-reactive) was performed at the end of ageing [6]. The non-reactive beam was subjected to the same moisture conditions as the reactive beam. This enabled the relevance of the model for simulating the residual resistance of these structures, when sound or damaged by ASR, to be assessed. It also

provided a complementary validation of the previous calculations because the stress and damage states, before these failure tests were performed, had a significant influence on the failure behaviour.

After 700 days, the beams were taken to failure with a 4-point flexural test using a slightly modified span (2.75 m vs. 2.8 m during the swelling phase) and supports on the underside (Figure 13).

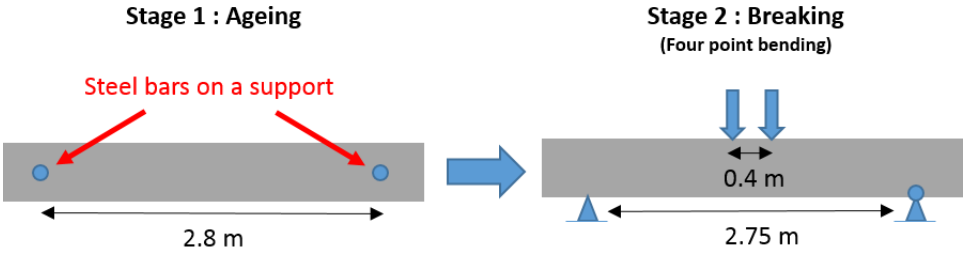

Figure 13: Mechanical limit conditions for the two stages: ageing and breaking

The steel behaviour was modelled using a bilinear law: a first elastic phase with a modulus of 200 GPa and an elastic limit at 500 MPa, and a second phase of hardening with a slope of 5 GPa (calibrated by inverse analysis of the non-reactive beam as no measurement of this data was performed during the experimental programme). In this phase, special care was taken concerning the anchoring of the steel bars: the mesh in the area of the supports was modified to simulate perfect anchoring. The calculation was carried out with a steel that was not under maximum strain (failure) and was thus stopped at the value of the force-deflection peak of the experimental curve (40 mm of deflection). Two main points were investigated in this work: the capability of the model to predict the first flexural cracks, and the load for structure yielding according to the stress and damage states due to ASR.

4.2. Deflections and applied load

Failure of the plain beams

The paper focuses on the flexural performance of reinforced concrete beams. But, as the model captures the concrete behaviour considering the combination of ASR, creep, shrinkage and mechanical damage, it is important to evaluate the capacity of the model to reproduce the performance of the two plain beams. The results of the failure tests for the beams without reinforcement is presented in Figure 14. The modulus of elasticity of the beam without ASR is 46,400 MPa to take into account the cement hydration in agreement with the conclusions of [6]. The behaviours of both beams are well-reproduced. The peak deflection of the non-reactive beam is a little too high (19%) but its rigidity is consistent. Without reinforcement, the ASR beam is weaker than the non-reactive one (experimentally 33%, numerically 45%). Indeed, the ASR damage reduces the mechanical characteristics such as the tensile strength. The rigidity of the ASR beam is a bit too low (25%) but the force peak is really consistent. The consideration of hydration could be a way of improvement for the modelling of these tests, in accordance with the conclusions of [6].

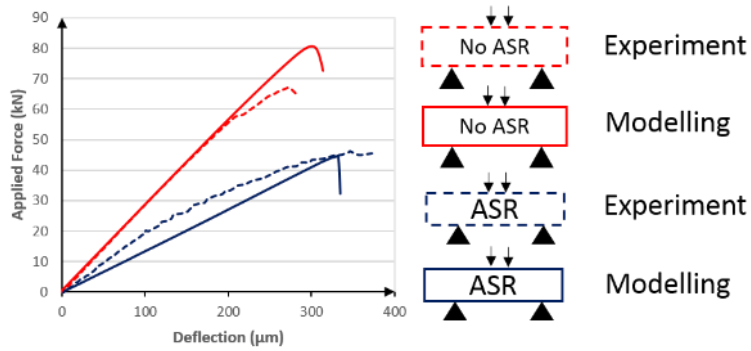

Figure 14: Force-Deflection curves of the failure test (model, theoretical results [6] and experiment [6] of the beams without reinforcement)

Failure of the non-reactive reinforced beam

Figure 15 compares the model responses with the experimental measurements given by [6]. For the non-reactive beam (red curves: experiment in dashed line and modelling in continuous line), the experimental data shows the first flexural tensile cracking at 75 kN and the steel

467 yielding at 150 kN. The model reproduces the structural behaviour correctly. The load for the
468 first flexural cracks is underestimated by about 20%: 60 kN for the first crack obtained by the
469 calculations. This can be explained by a slight overestimation of the impact on the failure
470 mode of cracks occurring on the upper face due to restrained shrinkage. The model seems to
471 slightly overestimate the rigidity at the beginning of the failure test. The yielding phase is well
472 reproduced. The stiffness differences after the first bending crack may be due to the
473 displacement of the sensor used to measure the deflection. The sensor was placed near a crack
474 (following the observations given in [6]).

475 *Failure of the reactive reinforced beams*

476 The reactive beam (dark blue curves: experiment in dashed line and modelling in continuous
477 line) follows the same evolution but the first flexural crack appears for a higher load (120 kN
478 versus 75 kN). The start of the steel yielding is similar to that for the non-reactive beam. The
479 experimental behaviour of the reactive beam is well reproduced throughout the test. The load
480 for the first flexural crack is slightly overestimated (140 kN versus 120 kN). In the
481 longitudinal direction of the reactive beam, there is no decrease in Young's modulus, thanks
482 to the anisotropic criteria. Thus, there is no loss of rigidity for the reactive beam, despite the
483 amount of expansion in the free direction.

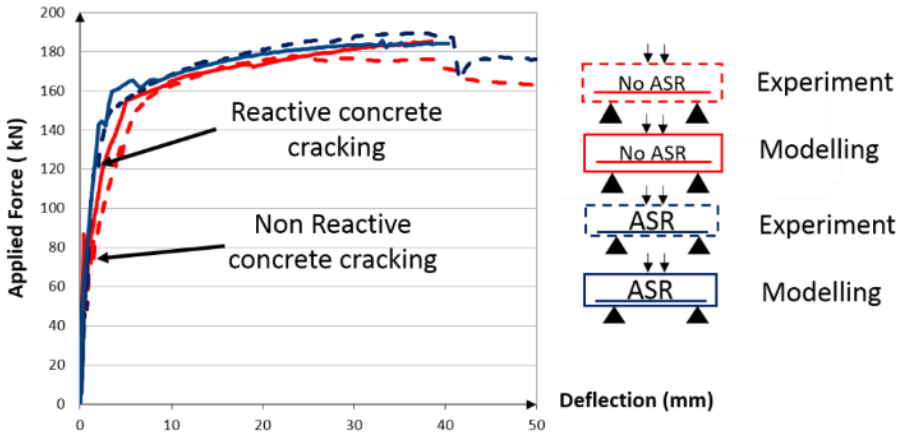

Figure 15: Force-Deflection curves of the failure test (model and experiment [6] of the normally reinforced beams)

The reactive beam cracking is delayed compared to the first cracking of the non-reactive beam. This is due to the chemical prestress developed in the concrete following the swelling restraint by the steel bars. For the reactive beam, the applied force is used first to decompress the concrete of the lower part before putting it in tension and cracking it. The difference of behaviour between the non-reactive and the reactive beams is well reproduced by the model even though the damage modelling needs to be improved to obtain more precise quantification.

The results of the failure test for the strongly reinforced beam is presented in Figure 16. The force - deflection curve obtained by the modelling is realistic until 13 mm of deflection. In this work, perfect bond has been assumed between steel and concrete. It is sufficient to reproduce the beams behaviour during the aging phase and the first part of the failure test (before large structural cracks). To obtain the final part of the curve and the possible concrete crushing, it is necessary to consider a more realistic bond slip behaviour.

The maximal stress reached in the stirrups during the aging and the failure tests is about 160 MPa. The mechanical behaviour of the stirrups is thus elastic during all the calculations.

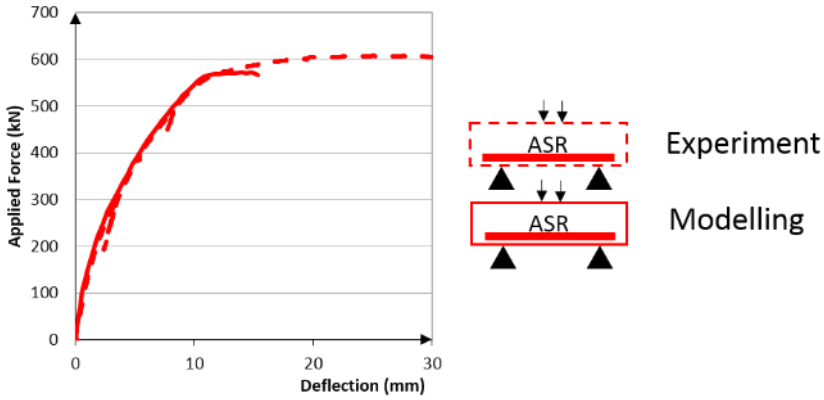

Figure 16: Force-Deflection curves of the failure test (model and experiment [6] of the strongly reinforced beam)

5. Discussion

Impact of ASR on the flexural performance of reinforced concrete beams

ASR seems beneficial to the bending behaviour of a reinforced beam. For the same applied force, the deflection is smaller for the reactive beam and cracking is delayed. This behaviour is particularly apparent for deflections of less than 5 mm. In the service limit state (SLS), the admissible force for these beams is 124 kN [6], corresponding to a deflection of 1.7 mm for the reactive beam and to a deflection to 3.9 mm for the non-reactive beam. This is an improvement of the flexural performance of the ASR beam due to the ASR-induced stress in the reinforced concrete (chemical prestress [54–56,4]) and to the anisotropic damage (no Young's modulus decrease in the longitudinal direction).

Impacts on durability

The structural cracking delay of the reinforced and reactive beam could imply a better protection from aggressive external agents (such as salts, sulfates or carbon dioxide) and water. However, diffuse cracking created parallel to the reinforcement due to ASR expansions facilitated their access. The durability of a beam, in particular of its reinforcement, which could become corroded faster, can therefore be affected. This aspect could largely balance the

positive effect of the chemical pre-stress mentioned above. A computational coupling of the state of cracking with a numerical model of corrosion by carbonation or sulfate attacks which would consider the consequences of longitudinal diffuse cracks on transfer properties could be a perspective on this point.

Minimum model skills to reproduce the improvement of the flexural behaviour

In order to reproduce the cracking delay of the ASR beam numerically, it is necessary to generate a good amplitude of ASR chemical prestress parallel to the reinforcement. Based on the above faithful modelling of this phenomenon, the capacities of the models necessary to obtain relevant quantification are established.

- The model used should be able to reproduce the anisotropy of the swelling in reinforced concrete to avoid cracking perpendicular to the reinforcements. An isotropic model will not be able to reproduce the cracking delay.
- The consistent amplitude of the ASR chemical prestress depends on the coupling between the pressure induced by ASR, the diffuse cracking in the unrestrained direction and the creep during the ageing stage.
- The model should be able to differentiate between the diffuse cracking (during ageing) and the structural cracking (during failure test).

6. Conclusion

The aim of this paper was to understand and model the impact of ASR on the flexural performance of reinforced concrete beams. A numerical approach was used to reproduce this behaviour and to discuss the real impact of ASR on reinforced concrete. The validation was performed on ageing structures in the laboratory. The simulation of the service life (ageing) and the residual strength (failure test) have been presented and analysed. The good

reproduction of the behaviour of the ASR reinforced beam allows some conclusions to be drawn:

1) First flexural cracks appear at higher load for ASR affected reinforced beam than for non-reactive, beam, due to the ASR chemical prestress generated by the restrained swelling in the reinforcement direction.
2) The rigidity of a reinforced beam is little impacted by ASR, due to anisotropic damage induced by the presence of the steel bars.
3) The cracking delay seems to be positive from the mechanical point of view. However, durability problems could appear because of the ASR diffuse cracking induced parallel to the reinforcement during the ageing phase. A corrosion model, coupled with a transfer model considering the cracking state could be a perspective on this point.
4) To reproduce the behaviour of reinforced concrete damaged by ASR numerically, models have to produce a realistic ASR chemical prestress in the reinforcement direction (coupling between ASR expansion, diffuse cracking and concrete creep) to evaluate the anisotropy of the mechanical properties, and to differentiate ASR diffuse cracking and structural macrocracks.

Acknowledgments

Financial support was provided by the Centre d'Ingénierie Hydraulique (CIH) of Electricité de France (EDF) in the framework of a PhD thesis approved by the French ANRT (Association Nationale de la Recherche et de la Technologie). This support is gratefully acknowledged.

REFERENCES

[1] P. Léger, P. Côté, R. Tinawi, Finite element analysis of concrete swelling due to alkali-aggregate reactions in dams, Computers & Structures. 60 (1996) 601–611. doi:10.1016/0045-7949(95)00440-8.

[2] S. Malla, M. Wieland, Analysis of an arch–gravity dam with a horizontal crack, Computers & Structures. 72 (1999) 267–278. doi:10.1016/S0045-7949(99)00033-4.

[3] B. Godart, M.R. de Rooij, J.G. Wood, Guide to Diagnosis and Appraisal of AAR Damage to Concrete in Structures, Springer, 2013.

[4] S. Ohno, Y. Yoshioka, Y. Shinozaki, T. Morikawa, The mechanical behaviour of reinforced of beams coated after Alkali-Silica Reaction damage, in: 8th International Conference on Alkali-Aggregate Reaction. Kyoto, Japan, 1989: pp. 697–702.

[5] F. Habibi, S.A. Sheikh, N. Orbovic, D.K. Panesar, F.J. Vecchio, Alkali aggregate reaction in nuclear concrete structures: part 3: structural shear wall elements, in: Structural Mechanics on Reactor Technology, Manchester, UK, 2015.

[6] S. Multon, Évaluation expérimentale et théorique des effets mécaniques de l'alcali-réaction sur des structures modèles, PhD thesis, Université de Marne-la-Vallée, 2003. http://www.theses.fr/2003MARN0181 (accessed March 14, 2016).

[7] S. Multon, J.-F. Seignol, E. Bourdarot, A. Jeanpierre, F. Toutlemonde, Effets structuraux de l'alcali-réaction: Apports d'une expérimentation sur éléments de structures à la validation de modèles, Revue Européenne de Génie Civil. 9 (2005) 1219–1247. doi:10.1080/17747120.2005.9692808.

[8] R.N. Swamy, Structural implications of alkali silica reaction, in: Proc. Of 8th International Conference on Alkali-Aggregate Reaction, Kyoto, Japan, 1989.

[9] W. Koyanagi, K. Rokugo, Y. Uchida, Mechanical properties of concrete deteriorated by alkali-aggregate reaction under various reinforcement ratios, in: Proceedings of the 9th International Conference on Alkali-Aggregate Reaction, 1992: pp. 556–563.

[10] C. Larive, Combined contribution of experiments and modeling to the understanding of alkali–aggregate reaction and its mechanical consequences, Laboratoire Central Des Ponts et Chaussées, Paris, France, Report OA. 28 (1998).

[11] B. Fournier, M.-A. Bérubé, Alkali-aggregate reaction in concrete: a review of basic concepts and engineering implications, Can. J. Civ. Eng. 27 (2000) 167–191. doi:10.1139/l99-072.

[12] A. Sellier, B. Capra, Modélisation physico-chimique de la réaction alcali-granulat: apport au calcul des structures dégradées, Revue Française de Génie Civil. 1 (1997) 445–481.

[13] E. Grimal, A. Sellier, S. Multon, Y. Le Pape, E. Bourdarot, Concrete modelling for expertise of structures affected by alkali aggregate reaction, Cement and Concrete Research. 40 (2010) 502–507. doi:10.1016/j.cemconres.2009.09.007.

[14] C. Comi, B. Kirchmayr, R. Pignatelli, Two-phase damage modeling of concrete affected by alkali–silica reaction under variable temperature and humidity conditions, International Journal of Solids and Structures. 49 (2012) 3367–3380.

[15] M. Alnaggar, G. Di Luzio, G. Cusatis, Modeling time-dependent behavior of concrete affected by alkali silica reaction in variable environmental conditions, Materials. 10 (2017) 471.

[16] A. Sellier, S. Multon, L. Buffo-Lacarrière, T. Vidal, X. Bourbon, G. Camps, Concrete creep modelling for structural applications: non-linearity, multi-axiality, hydration,

611 temperature and drying effects, Cement and Concrete Research. 79 (2016) 301–315.
612 doi:10.1016/j.cemconres.2015.10.001.
613 [17] P. Morenon, S. Multon, A. Sellier, E. Grimal, F. Hamon, E. Bourdarot, Impact of stresses
614 and restraints on ASR expansion, Construction and Building Materials. 140 (2017) 58–
615 74. doi:10.1016/j.conbuildmat.2017.02.067.
616 [18] O. Coussy, Mécanique des milieux poreux, Editions Technip, 1991.
617 [19] M.A. Biot, General Theory of Three-Dimensional Consolidation, Journal of Applied
618 Physics. 12 (1941) 155–164. doi:10.1063/1.1712886.
619 [20] J. Pan, Y. Feng, F. Jin, Y. Xu, Q. Sun, C. Zhang, D. Owen, Meso-scale particle modeling of
620 concrete deterioration caused by alkali-aggregate reaction, International Journal for
621 Numerical and Analytical Methods in Geomechanics. 37 (2013) 2690–2705.
622 [21] M. Alnaggar, G. Cusatis, G.D. Luzio, Lattice Discrete Particle Modeling (LDPM) of Alkali
623 Silica Reaction (ASR) deterioration of concrete structures, Cement and Concrete
624 Composites. 41 (2013) 45–59. doi:10.1016/j.cemconcomp.2013.04.015.
625 [22] L.F.M. Sanchez, B. Fournier, M. Jolin, J. Duchesne, Reliable quantification of AAR
626 damage through assessment of the Damage Rating Index (DRI), Cement and Concrete
627 Research. 67 (2015) 74–92. doi:10.1016/j.cemconres.2014.08.002.
628 [23] A. Sellier, Anisotropic Damage and Visco-Elasto-Plasticity Applied to Multiphasic
629 Materials, LMDC - Laboratoire Matériaux et Durabilité des Constructions de Toulouse ;
630 Université de Toulouse III - Paul Sabatier ; INSA de Toulouse, 2018. https://hal-insa-
631 toulouse.archives-ouvertes.fr/hal-01710289/document (accessed February 21, 2018).
632 [24] E. Grimal, A. Sellier, Y. Le Pape, E. Bourdarot, Creep, Shrinkage, and Anisotropic Damage
633 in Alkali-Aggregate Reaction Swelling Mechanism-Part I. A Constitutive Model, ACI
634 Materials Journal. 105 (2008) 227–235.
635 [25] C. Larive, Apports combinés de l'expérimentation et de la modélisation à la
636 compréhension de l'alcali-réaction et de ses effets mécaniques, PhD thesis, Ecole
637 Nationale des Ponts et Chaussées, 1997. https://pastel.archives-ouvertes.fr/tel-
638 00520676/document (accessed May 3, 2016).
639 [26] S. Poyet, Sellier, A., Capra, B., Thèvenin-Foray, G., Torrenti, J.M., Tournier-Cognon, H.,
640 Bourdarot, E., Influence of Water on Alkali-Silica Reaction: Experimental Study and
641 Numerical Simulations, Journal of Materials in Civil Engineering. 18 (2006) 588–596.
642 doi:10.1061/(ASCE)0899-1561(2006)18:4(588).
643 [27] G.W. Scherer, Freezing gels, Journal of Non-Crystalline Solids. 155 (1993) 1–25.
644 [28] B. Zuber, J. Marchand, Predicting the volume instability of hydrated cement systems
645 upon freezing using poro-mechanics and local phase equilibria, Materials and
646 Structures. 37 (2004) 257.
647 [29] J. Ponce, O.R. Batic, Different manifestations of the alkali-silica reaction in concrete
648 according to the reaction kinetics of the reactive aggregate, Cement and Concrete
649 Research. 36 (2006) 1148–1156.
650 [30] L.J. Struble, S. Diamond, Swelling properties of synthetic alkali silica gels, Journal of the
651 American Ceramic Society. 64 (1981) 652–655.
652 [31] E. Garcia-Diaz, J. Riche, D. Bulteel, C. Vernet, Mechanism of damage for the alkali–silica
653 reaction, Cement and Concrete Research. 36 (2006) 395–400.
654 [32] A.G. Vayghan, F. Rajabipour, J.L. Rosenberger, Composition–rheology relationships in
655 alkali–silica reaction gels and the impact on the gel's deleterious behavior, Cement and
656 Concrete Research. 83 (2016) 45–56.

[33] A. Sellier, J.P. Bournazel, A. Mébarki, Une modélisation de la réaction alcalis-granulat intégrant une description des phénomènes aléatoires locaux, Materials and Structures. 28 (1995) 373–383.
[34] J. Liaudat, I. Carol, C.M. López, V.E. Saouma, ASR expansions in concrete under triaxial confinement, Cement and Concrete Composites. (2017). doi:10.1016/j.cemconcomp.2017.10.010.
[35] L. Sanchez, B. Fournier, M. Jolin, J. Duchesne, Reliable quantification of AAR damage through assessment of the Damage Rating Index (DRI), Cement and Concrete Research. 67 (2015) 74–92.
[36] B. Capra, A. Sellier, Orthotropic modelling of alkali-aggregate reaction in concrete structures: numerical simulations, Mechanics of Materials. 35 (2003) 817–830.
[37] B. Capra, A. Sellier, Anisotropic modelling of alkali–aggregate reaction in concrete, in: 11th Int. Conf. on AAR, Quebec City, 2000: pp. 929–938.
[38] I. Carol, Z.P. Bazant, Damage and plasticity in microplane theory, International Journal of Solids and Structures. 34 (1997) 3807–3835. doi:10.1016/S0020-7683(96)00238-7.
[39] A.D. Jefferson, Craft—a plastic-damage-contact model for concrete. I. Model theory and thermodynamic considerations, International Journal of Solids and Structures. 40 (2003) 5973–5999.
[40] A. Sellier, G. Casaux-Ginestet, L. Buffo-Lacarrière, X. Bourbon, Orthotropic damage coupled with localized crack reclosure processing. Part I: Constitutive laws, Engineering Fracture Mechanics. 97 (2013) 148–167. doi:10.1016/j.engfracmech.2012.10.012.
[41] S. Rahal, A. Sellier, G. Casaux-Ginestet, Finite element modelling of permeability in brittle materials cracked in tension, International Journal of Solids and Structures. 113 (2017) 85–99. doi:10.1016/j.ijsolstr.2016.12.023.
[42] A. Hillerborg, M. Modéer, P.-E. Petersson, Analysis of crack formation and crack growth in concrete by means of fracture mechanics and finite elements, Cement and Concrete Research. 6 (1976) 773–781. doi:10.1016/0008-8846(76)90007-7.
[43] S. Multon, F. Toutlemonde, Effect of moisture conditions and transfers on alkali silica reaction damaged structures, Cement and Concrete Research. 40 (2010) 924–934. doi:10.1016/j.cemconres.2010.01.011.
[44] S. Multon, F. Toutlemonde, Water distribution in concrete beams, Mat. Struct. 37 (2004) 378. doi:10.1007/BF02479634.
[45] F. Bangert, D. Kuhl, G. Meschke, Chemo-hygro-mechanical modelling and numerical simulation of concrete deterioration caused by alkali-silica reaction, International Journal for Numerical and Analytical Methods in Geomechanics. 28 (2004) 689–714.
[46] S. Rahal, A. Sellier, J. Verdier, Modelling of change in permeability induced by dilatancy for brittle geomaterials, Construction and Building Materials. 125 (2016) 613–624.
[47] S. Poyet, Etude de la degradation des ouvrages en beton atteints par la reaction alcali-silice - approche experimentale et modelisation numerique des degradations dans un environnement hydro-chemo-mecanique variable, PhD thesis, Université de Marne la Vallée, 2003. https://tel.archives-ouvertes.fr/tel-00006479/document (accessed July 31, 2017).
[48] R. Mensi, P. Acker, A. Attolou, Séchage du béton: analyse et modélisation, Materials and Structures. 21 (1988) 3–12. doi:10.1007/BF02472523.
[49] P. Morenon, Modélisation des réactions de gonflement interne des bétons avec prise en compte des couplages poro-mécaniques et chimiques, Université de Toulouse, Université Toulouse III - Paul Sabatier, 2017.

[50] K.K. Aligizaki, Pore structure of cement-based materials: testing, interpretation and requirements, CRC Press, 2005.
[51] W. Koyanagi, K. Rokugo, H. Ishida, Failure Behavior of Reinforced Concrete Beams Deteriorated by Alkali-Silica Reactions, in: Proc. 7th Int. Conf. on AAR, Ottawa, 1986: pp. 141–145.
[52] L.J. Monette, N.J. Gardner, P.E. Grattan-Bellew, Residual strength of reinforced concrete beams damaged by alkali-silica reaction—Examination of damage rating index method, Materials Journal. 99 (2002) 42–50.
[53] S. Multon, J.-F. Seignol, Toutlemonde François, Chemomechanical Assessment of Beams Damaged by Alkali-Silica Reaction, Journal of Materials in Civil Engineering. 18 (2006) 500–509. doi:10.1061/(ASCE)0899-1561(2006)18:4(500).
[54] M. Fujii, K. Kobayashi, T. Kojima, H. Maehara, The static and dynamic behavior of reinforced concrete beams with cracking due to alkali–silica reaction, in: 7th International Conference on Alkali-Aggregate Reactions, Ottawa, Canada, 1986: pp. 126–130.
[55] S. Inoue, M. Fujii, K. Kobayashi, K. Nakano, Structural behaviors of reinforced concrete beams affected by alkali–silica reaction, in: Proceedings of the 8th International Conference on Alkali–Aggregate Reaction in Concrete, Kyoto, Japan, 1989: pp. 17–20.
[56] L.A. Clark, Critical review of the structural implications of the alkali silica reaction in concrete, Bridges Design, Structures Group, Transportation andRoad Research Laboratory, 1989.